Counter-rotation and High-velocity Outflow in the Parsec-scale Molecular Torus of NGC 1068

C. M. Violette Impellizzeri[1,2] , Jack F. Gallimore[3] , Stefi A. Baum[4] , Moshe Elitzur[5] , Richard Davies[6] , Dieter Lutz[6] ,
Roberto Maiolino[7] , Alessandro Marconi[8,9] , Robert Nikutta[10] , Christopher P. O'Dea[4] , and Eleonora Sani[11]

[1] Joint ALMA Observatory, Alonso de Cordova 3107, Vitacura, Santiago, Chile; Violette.Impellizzeri@alma.cl
[2] National Radio Astronomy Observatory, 520 Edgemont Road, Charlottesville, VA 22903, USA
[3] Department of Physics and Astronomy, Bucknell University, Lewisburg, PA 17837, USA
[4] University of Manitoba, Department of Physics and Astronomy, Winnipeg, MB R3T 2N2, Canada
[5] Astronomy Department, University of California, Berkeley, CA 94720, USA
[6] Max Planck Institute for Extraterrestrial Physics, Giessenbachstrasse 1, D-85748 Garching, Germany
[7] Kavli Institute for Cosmology, University of Cambridge, Madingley Road, Cambridge CB3 0HA, UK
[8] Dipartimento di Fisica e Astronomia, Universit'a di Firenze, via G. Sansone 1, I-50019, Sesto Fiorentino (Firenze), Italy
[9] INAF-Osservatorio Astrofisico di Arcetri, Largo E. Fermi 5, 50135, Firenze, Italy
[10] National Optical Astronomy Observatory, 950 North Cherry Avenue, Tucson, AZ 85719, USA
[11] European Southern Observatory, Alonso de Cordova 3107, Vitacura, Santiago, Chile

Abstract

We present 1.4 pc resolution observations of 256 GHz nuclear radio continuum and HCN ($J = 3 \rightarrow 2$) in the molecular torus of NGC 1068. The integrated radio continuum emission has a flat spectrum consistent with free–free emission and resolves into an X-shaped structure resembling an edge-brightened bicone. HCN is detected in absorption against the continuum, and the absorption spectrum shows a pronounced blue wing that suggests a high-velocity molecular outflow with speeds reaching 450 km s^{-1}. Analysis of the off-nucleus emission line kinematics and morphology reveals two nested, rotating disk components. The inner disk, inside $r \sim 1.2$ pc, has kinematics that are consistent with the nearly edge-on, geometrically thin H$_2$O megamaser disk in Keplerian rotation around a central mass of $1.66 \times 10^7 M_\odot$. The outer disk, which extends to ∼7 pc radius, counter-rotates relative to the inner disk. The rotation curve of the outer disk is consistent with rotation around the same central mass as the megamaser disk but in the opposite sense. The morphology of the molecular gas is asymmetric around the nuclear continuum source. We speculate that the outer disk formed from more recently introduced molecular gas falling out of the host galaxy or from a captured dwarf satellite galaxy. In NGC 1068, we find direct evidence that the molecular torus consists of counter-rotating and misaligned disks on parsec scales.

Key words: galaxies: active – Interstellar medium – quasars: supermassive black holes – Radio interferometry – Seyfert galaxies

1. Introduction

The unifying model for active galaxies holds that all active galactic nuclei (AGNs) are powered by accretion onto a supermassive black hole (SMBH; Antonucci 1993; Ramos Almeida & Ricci 2017; Hickox & Alexander 2018). The accretion disk and broad-line region (BLR) are surrounded by a dusty, molecular medium, commonly referred to as the "obscuring torus." The torus selectively obscures sight-lines to the central engine, resulting in a dichotomy of AGN spectra. If the torus is viewed more nearly pole-on, we can see the BLR and classify the AGN as type 1; if the torus is viewed more nearly edge-on, the BLR may be obscured and the AGN is classified as type 2 (Lawrence & Elvis 1982). A parsec-scale torus must be geometrically thick to explain the large detection fraction of type 2 AGNs (Osterbrock & Shaw 1988; Tovmassian 2001).

NGC 1068 is one of the nearest, luminous Seyfert type 2 galaxies and has served as an archetype for unifying schemes (Antonucci & Miller 1985). Polarimetry of the reflected nuclear spectrum reveals the hidden BLR and ultraviolet (UV) continuum source (Antonucci & Miller 1985; Capetti et al. 1995; Inglis et al. 1995). The Seyfert nucleus of NGC 1068 is obscured by a dusty, molecular medium (Mason et al. 2006; Gallimore et al. 2016; García-Burillo et al. 2016; Imanishi et al. 2018). A flat spectrum radio source, "S1," marks the location

of the central engine (Gallimore et al. 1996; Muxlow et al. 1996). Very Long Baseline Array (VLBA) continuum observations resolve the continuum source into an elongated, pc-scale structure oriented nearly at right angles to the kpc-scale radio jet; the radio source has been interpreted as a plasma disk located inside the obscuring molecular medium (Gallimore et al. 1997, 2004). The cm-wave continuum source associates with the disk of H$_2$O vapor megamaser emission with systemic velocity 1130 km s^{-1} (optical convention, LSRK reference frame) and maximum rotation speed 335 km s^{-1} at a distance of 0.6 pc from the central engine (Greenhill & Gwinn 1997; Gallimore et al. 2001; Gallimore & Impellizzeri 2019).

Recent Atacama Large Millimeter/submillimeter Array (ALMA) observations of the molecular interstellar medium (ISM) in the central few pc have revealed complicated kinematics (Gallimore et al. 2016; García-Burillo et al. 2016; Imanishi et al. 2018). With a ∼ 3 pc (0″04) beam,[12] ALMA observations of CO ($J = 6 \rightarrow 5$) and HCN ($J = 3 \rightarrow 2$) resolve an extended, roughly 10 pc by 4 pc distribution of molecular gas oriented nearly at right angles to the radio jet axis but nearly aligned with the major axis of the nuclear plasma disk, S1. We found evidence for high-velocity CO in a

---

[12] We adopt the Ringberg Standards for NGC 1068 (Bland-Hawthorn et al. 1997), which assigns the scale 1″ = 70 pc.

bipolar outflow, with radial velocities ranging to ± 400 km s^{-1} relative to systemic, in the central pc (Gallimore et al. 2016). Imanishi et al. observed HCN ($J = 3 \rightarrow 2$) at ~3 pc resolution, and they argued that, unlike CO ($J = 6 \rightarrow 5$), the molecular gas traced by HCN better traces the rotational, disk-like region of the torus. However, they also argue that the kinematics are not consistent with pure rotation but show evidence for significant turbulence (i.e., enhanced velocity dispersion revealed by the second spectral moment) and perhaps counter-rotation compared to the molecular gas on hundred parsec scales.

In an effort to untangle the complicated geometry and kinematics of the molecular torus of NGC 1068, we obtained new ALMA observations of HCN ($J = 3 \rightarrow 2$) at 1.4 pc (20 mas) resolution. The observations and data reduction are summarized in Section 2. The main results, including moment maps and a kinematic analysis, are presented in Section 3. We summarize our main conclusions in Section 4.

2. Observations and Data Reduction

We used ALMA to observe NGC 1068 in Band 6 during ALMA Cycle 5 (project code 2017.1.01666.S). We used the longest baseline configuration available for Band 6 during Cycle 5, C43-10, with baselines ranging from 41.4 m to 16.2 km. The largest recoverable structure is about 0″32, or 22 pc at the distance of NGC 1068. The source was observed in nine execution blocks between 2017 October 10 and 2017 October 24. The average exposure time per execution block was 1.6 hr, and the total integration time on source was 14.5 hr. Source observations were interleaved with short scans of nearby bright calibrator sources. The phase calibrator was J0239−0234, located 2°7 from NGC 1068, and the flux calibrator was J0432−0120, with flux density $S_\nu = 0.97 \pm 0.04$ Jy.

Spectral windows were tuned to observe three continuum windows, 1.875 GHz total bandwidth each and one tuned to observe HCN ($J = 3 \rightarrow 2$; $\nu_0 = 265.88618$ GHz) at recessional velocity 1150 km s^{-1} (optical convention, LSRK reference frame). The HCN line observation has channel-width ~1.0 km s^{-1} and spans ~1000 km s^{-1} total bandwidth.

The data were calibrated using CASA pipeline version 40896 (Pipeline-CASA51-P2-B) and imaged using CASA 5.1.1 (McMullin et al. 2007). We performed four cycles of phase-only self-calibration on the continuum data (Cornwell & Fomalont 1989), and the solutions were applied to the spectral line data. The visibility data were Briggs-weighted during Fourier inversion (Briggs 1995). The spectral line data were averaged in frequency to provide approximately 10 km s^{-1} wide channels. Continuum subtraction of the line data was performed in the (u, v) plane using an average of channels with radial velocities |RV| > 600 km s^{-1} relative to systemic. The common restoring beam is 19.9×19.1 mas, PA 79°8, and the median line channel sensitivity is 1.6 mJy beam^{-1}.

The continuum image was produced by combining all continuum channels into a single image at effective $\nu = 256.5$ GHz (multi-frequency synthesis; Sault & Conway 1999). The restoring beam of the continuum image is 20.2×19.6 mas, PA 78°3, and the rms sensitivity is 6.2 μJy beam^{-1}.
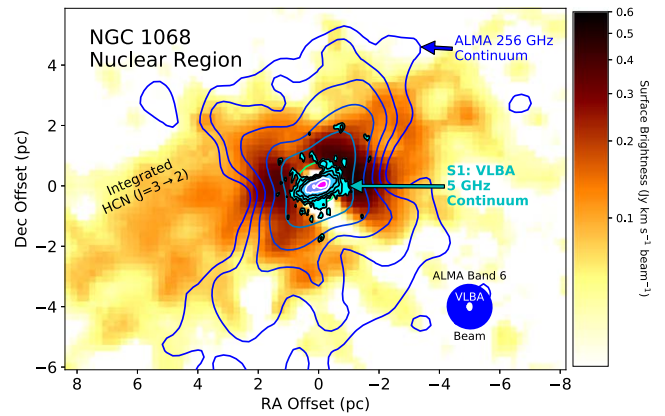

Figure 1. Nuclear region of NGC 1068 shown as overlays of the ALMA 256 GHz continuum (blue–green unfilled contours; Band 6), VLBA 5 GHz continuum (black contours filled with shades of cyan to magenta; Gallimore et al. 2004), and ALMA integrated HCN ($J = 3 \rightarrow 2$; Band 6; background image in shades of yellow to dark red). A compact source model for S1 has been subtracted from the ALMA continuum; the flux density of the compact source is 6.6 ± 0.3 mJy. The Band 6 contour continuum levels are (blue) 0.019, 0.037, 0.075, 0.15, (blue–green) 0.30, and (green, mostly obscured by the VLBA continuum contours) 0.60 mJy beam^{-1}. The integrated HCN image is shown with an arcsinh stretch and surface brightness limits 0.004 (5σ) to 0.6 Jy km s^{-1} beam^{-1}. Blanked values (<5σ) display as white.

3. Results

Figure 1 presents images of the HCN ($J = 3 \rightarrow 2$) integrated line flux and 256 GHz continuum. The line is detected in absorption at the position of S1, and the brightest integrated emission extends about 7 pc from S1 both southeast and northwest of S1. ALMA resolves the integrated HCN emission, with surface brightness (uncorrected for absorption) peaking roughly 2 pc to either side of S1 and fading with distance from S1. The morphology is irregular, suggesting substructure on scales at least as small as the ~1.4 pc beam. The orientation of the HCN major axis is PA ~114°, estimated by drawing a line through the continuum peak and between the outer contours of the integrated HCN flux map. Image moment analysis agrees with this estimate of the major axis orientation to within ~5°, which corresponds to a difference of less than half of a beam at the extent of the major axis. The major axis is more closely aligned with the milliarcsecond-scale radio continuum structure of S1 but nearly perpendicular to the radio jet on 100 pc scales.

At lower surface brightness levels, the ALMA 256 GHz continuum image resolves into an X-shaped structure that resembles a bicone extending perpendicular both to the molecular gas distribution and the major axis of the VLBA continuum source. We have interpreted the VLBA continuum source as arising from a parsec-scale plasma disk (Gallimore et al. 2004). That the major axis of the fainter ALMA continuum emission aligns nearly perpendicular to the VLBA major axis is consistent with a disk-bicone scenario. On the sub-pc scale, the VLBA continuum contours also show X-shaped extensions away from the plasma disk plane that appear to line up roughly with the ALMA continuum extensions. Although a detailed analysis of the continuum is outside the scope of this Letter, we note that the 256 GHz continuum is probably dominated by free–free emission. The integrated flux density of the S1 region in a 0″13 (9.1 pc) square aperture is 12.7 ± 0.1 mJy. Based on the Very Large Array (VLA) 43 GHz measurement of Cotton et al. (2008) and
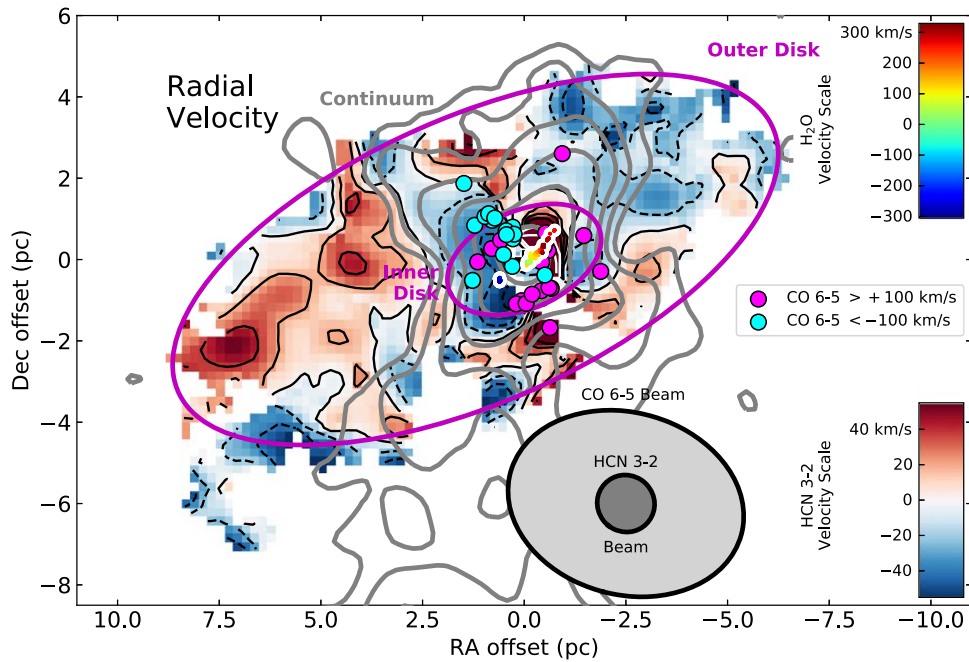
Figure 2. Radial velocities of molecular gas in the nuclear region of NGC 1068. The systemic velocity, 1130 km s^{-1} (LSRK, optical convention; Gallimore & Impellizzeri 2019), has been subtracted from the radial velocities. Included in this figure are the H$_2$O megamaser spots (colored spots outlined in white; Greenhill & Gwinn 1997), the 256 GHz continuum (gray contours as in Figure 1), the velocity map of HCN $J = 3 \rightarrow 2$ (black contours with red–blue shading), and spots marking the peak surface brightness emission of high-velocity CO ($J = 6 \rightarrow 5$) (Gallimore et al. 2016; magenta and cyan filled circles). The velocity contours run from -60 km s^{-1} to $+60$ km s^{-1} in steps of 20 km s^{-1}; negative velocities are contoured with dashed lines. The regions identified as the inner and outer counter-rotating disks are outlined by annotated, magenta ellipses.

assuming a 5% uncertainty in the flux scale, the continuum spectral index is $\alpha = -0.06 \pm 0.03$ ($S_\nu \propto \nu^\alpha$; 1σ uncertainty). Accepting additional uncertainty owing to the difference in resolution (80 mas for the VLA), this measurement is consistent with the spectral index expected for optically thin free–free emission, $\alpha = -0.1$.

We measured the radial velocity field of the spectral line cube using Gauss–Hermite polynomial fits to each spectrum in the HCN datacube (see van der Marel & Franx 1993 for a description of this technique); the result is shown in Figure 2. Outside of about 1 pc projected radius, the broad trend is redshifts relative to systemic on the eastern side and blueshifts on the western side. The kinematics are consistent with the results presented by Imanishi et al. (2018) but opposite the sense of motion of the H$_2$O masers (Greenhill & Gwinn 1997). Inside the central parsec, however, the kinematics more closely resemble the H$_2$O megamaser disk, with high-velocity redshifted HCN northwest of the nucleus and high-velocity blueshifted HCN southeast of S1.

The rotating disk(s) interpretation is complicated by the velocity field northeast and southwest of the nucleus, which does not cleanly resolve from the near-nuclear gas. This axis coincides with the bipolar outflow seen in CO ($J = 6 \rightarrow 5$; Gallimore et al. 2016), and so we speculate the complex radial velocity field northeast and southwest of the nucleus results from a beam-convolved blend of clouds in the rotating disk and clouds participating in the outflow. Supporting this picture, we find that the high-velocity HCN ($J = 3 \rightarrow 2$) appears to bracket the CO ($J = 6 \rightarrow 5$) outflow. The simplest interpretation would have the HCN trace molecular gas in a rotating disk that collimates the molecular outflow detected in CO ($J = 6 \rightarrow 5$) emission and evidenced by the disturbed HCN radial velocities along the minor axis.

The nuclear absorption profile, provided in Figure 3, shows additional evidence for an outflow component in HCN ($J = 3 \rightarrow 2$). We extracted the nuclear spectrum at the position of the nuclear radio source S1. To estimate a correction for line emission in the beam, we averaged the spectra from positions 1.4 pc (one beam) northeast and southwest of the nucleus and subtracted the result from the nuclear spectrum. The resulting corrected absorption profile shows a minimum centered near the systemic velocity, as expected for an edge-on, rotating disk surrounding the nuclear continuum source. However, the line profile is asymmetric: there is a pronounced blue wing on the absorption profile that extends to roughly -450 km s^{-1} relative to systemic. The blue wing appears on both the raw and corrected spectra, and so it is likely not an artifact of the emission correction. For comparison, the maximum rotation speed of the inner disk is $\sim$380 km s^{-1} (see below). The excess blueshifted absorption is consistent with outflow velocities approaching 450 km s^{-1}, exceeding the 400 km s^{-1}, maximum outflow velocities observed in CO ($J = 6 \rightarrow 5$) line emission (Gallimore et al. 2016).

Position–velocity diagrams along the major (PA 114°) and minor (PA 24°) axes are shown in Figure 4. On the major axis diagram, the highest velocity emission agrees with the positional offsets and range of velocities spanned by the redshifted H$_2$O masers (see also Figure 2) and so likely arises from the inner disk. Within offsets $\lesssim$3 pc, the region of the brightest continuum emission, the brightest HCN line emission spans radial velocities -170 to 100 km s^{-1} relative to systemic. Given the coincidence with the radio continuum and the presence of both redshifted and blueshifted emission, we interpret this region as including a significant contribution from spatially unresolved molecular outflow, which is consistent with our interpretation of the velocity map (Figure 2). The
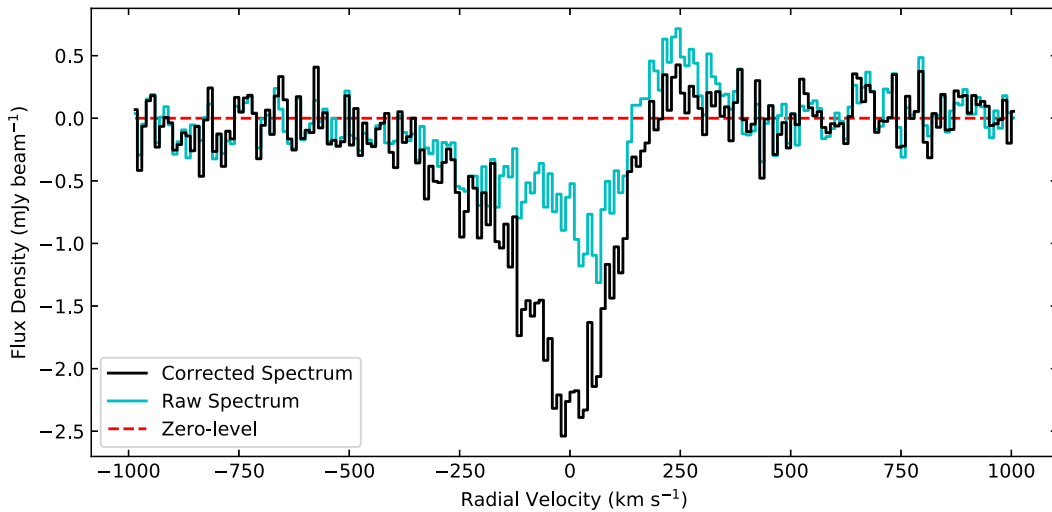
Figure 3. Continuum-subtracted nuclear absorption profile of HCN ($J = 3 \rightarrow 2$). The raw spectrum is plotted in cyan, the spectrum corrected for line emission is plotted in black, and the red dashed line shows the zero-level. The systemic velocity, 1130 km s^{-1} (LSRK, optical convention; Gallimore & Impellizzeri 2019), has been subtracted from the radial velocities.

outflow emission is most likely overlapping with some of the higher-velocity rotating gas. The presence of both redshifted and blueshifted emission suggests a biconical outflow with an outflow axis aligned near the plane of the sky (see Das et al. 2006). For offsets $\gtrsim 4$ pc, the emission is preferentially redshifted to the southeast and blueshifted to the northwest, as is evident on the velocity map (Figure 2). This region appears to be well separated from the outflow region and runs roughly orthogonal to the known outflow and jet axes. Although some beam-smeared outflow emission may contribute to this outer region, it seems more likely that rotation dominates the kinematics of the outer part of the HCN emission along the major axis.

The minor axis position–velocity diagram places some constraints on the scale of the outflow. Allowing for beam-smearing, HCN ($J = 3 \rightarrow 2$) emission extends roughly 1 pc northeast of the nucleus, but the HCN emission is much weaker to the southwest (see Figure 1). The CO ($J = 6 \rightarrow 5$) emission similarly spans roughly 1–2 pc both southwest and northeast of the nucleus. Of course, the presence of line absorption, sensitivity limitations, and, potentially, confusion with over-lapping emission from the inner disk complicate the measure-ment of the extent of the molecular outflow in HCN. On the other hand, molecular gas lifted from the shielding of the nuclear disk(s) would be soon exposed to the ionizing continuum from the AGN, and we speculate that the molecular outflow might become ionized and feed into to the larger, $\sim$400 pc ionized gas outflow (see Cecil et al. 1990). The implication would be acceleration from maximum line-of-sight velocities of roughly 450 km s^{-1} for outflowing molecular clouds (Figure 3) to 1000 km s^{-1} for [O III] emission line clouds within the central 14 pc (Das et al. 2006).

We measured the parsec-scale rotation curve from the HCN ($J = 3 \rightarrow 2$) data using the conventional tangential velocity technique (Kerr & Westerhout 1965). To perform this analysis, we used an automated numerical technique to determine the tangential velocity as a function of offset along the major axis of the integrated HCN map. For projected $r \geqslant 1.2$ pc, we extracted spectra at each pixel along the major axis (1 pixel = 0.2 pc). For $r < 1.2$ pc, we instead extracted two spectra, one northwest of the nucleus and one southeast along

the axis defined by the maser spot distribution (PA 131°) and at the locations of the brightest peak line emission in that region. The northeast spectrum was extracted at a position located $r = 0.5$ pc from the nuclear continuum source. Owing to confusion with the blue wing of the nuclear absorption line, the extraction for the southeast position is farther from the nucleus, at projected radius $r = 0.9$ pc.

A Gauss–Hermite polynomial was fitted to each extracted HCN spectrum, and Monte Carlo realizations of the spectrum were generated by adding a randomly generated noise spectrum scaled to the observed rms. The procedure next bracketed the region surrounding the spectral peak and the nearest velocity where the simulated spectrum falls below the background noise. The average and standard deviation of 10^4 trials, respectively, provide an estimate of the tangential velocity and its uncertainty. The median uncertainty is 30 km s^{-1}. Note that this method does not correct for the unknown, intrinsic velocity dispersion of the gas. However, intrinsic velocity dispersions as high as $\sigma_r = 90$ km s^{-1}, comparable to the inferred rotation speeds, introduce corrections that are smaller than the measurement uncertainties.

The results are shown in Figure 4, which also includes the radial velocities of the nuclear H$_2$O megamasers and the Keplerian rotation curve that best fits the H$_2$O megamaser kinematics (Gallimore & Impellizzeri 2019).

The $r > 1.2$ pc rotation curve is consistent with an extrapolation of the Keplerian rotation curve. There are bumps and wiggles that deviate slightly from Keplerian rotation perhaps owing to confusion with the molecular outflow, i.e., overlap between the outflow and rotating gas within our beam; however, from inspection of Figure 4, these deviations are small compared to the measurement uncertainties. More specifically, the largest statistical deviation from the predicted Keplerian rotation curve is located 3.4 pc northwest of the nucleus. There, the measured rotational speed deviates from the predicted Keplerian rotation curve by 70 ± 40 km s^{-1}, which is a $<2\sigma$ deviation.

Again we emphasize that, between $r = 1.2$ pc and $r \sim 7$ pc, the outer HCN rotation curve runs counter to the inner maser disk rotation; that is, the masers recede toward the northwest, but the outer HCN disk recedes to the southeast. However,
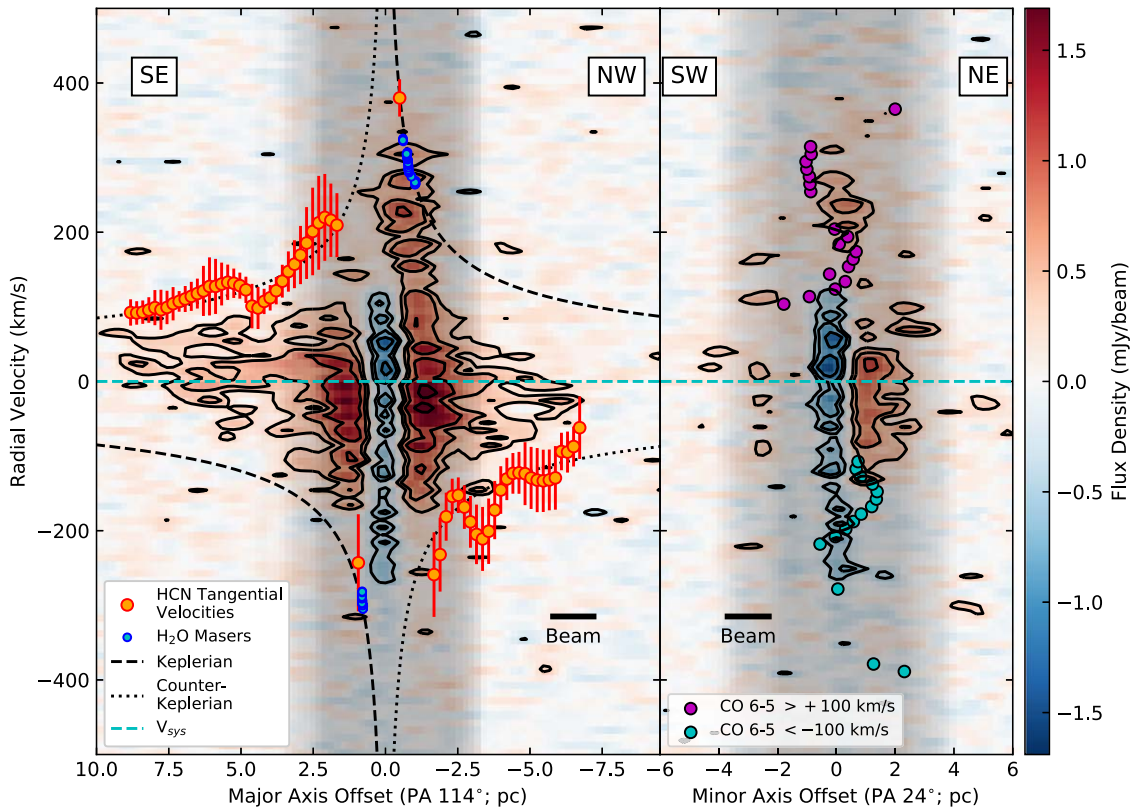
Figure 4. ALMA HCN ($J = 3 \rightarrow 2$) position–velocity diagrams extracted along the HCN major axis (left panel) and minor axis (right panel). The radial velocities are offset relative to systemic, 1130 km s^{-1} (LSRK, optical convention; Gallimore & Impellizzeri 2019) , which is marked by the blue–green dashed line. The major axis offsets run southeast (positive offset) to northwest (negative offset) along PA 114° through the nuclear continuum source S1, and the minor axis offsets run southwest (negative offset) to northeast (positive offset) along PA 24°. The contour levels run from -1.6 to 1.6 mJy beam^{-1} in steps of 0.4 mJy beam^{-1}. On the major axis diagram, the tangential HCN velocities are marked by yellow dots with red errorbars, and, for comparison, the H$_2$O maser radial velocities along PA $\sim$131° are shown as filled blue circles (data from Greenhill & Gwinn 1997) corrected for the best-fit inclination, $i = 79°$. The best-fitting model for the H$_2$O masers, shown with a dashed line, is Keplerian rotation around a central mass of $1.66 \times 10^7\ M_\odot$ (inner disk rotation; Gallimore & Impellizzeri 2019). The dotted line shows the same Keplerian rotation, but in the opposite sense. The 256 GHz continuum emission is indicated by the shaded gray regions. The grayscale stretch runs between 16 and 50 mJy beam^{-1}.

inside $r = 1.2$ pc, the HCN rotation follows the sense of the maser disk rotation. The inferred rotation speeds of the inner HCN disk reach 380 ± 30 km s^{-1}, exceeding the maximum rotation speed of the H$_2$O megamaser disk, 335 km s^{-1}. This result suggests that we have detected molecular gas closer to the central engine than the gas traced by the H$_2$O megamasers. Note also that the masers align along PA 131° (from the nucleus toward the approaching masers; Gallimore & Impellizzeri 2019), misaligned from the integrated, larger-scale HCN major axis by nearly 20°.

4. Conclusions

We used ALMA to observe 256 GHz continuum and the transition HCN ($J = 3 \rightarrow 2$) at roughly parsec resolution in the molecular torus of NGC 1068. Comparing to VLA 43 GHz measurements, the continuum has a flat spectrum that is consistent with free–free emission. The continuum structure resembles a bicone viewed from the side, perpendicular to the symmetry axis.

Turning to the HCN observations, we identify three kinematically distinct regions: (1) an outflow component apparent in emission on the HCN position–velocity diagram and detected as a blueshifted wing in absorption against the nuclear continuum source, with projected outflow speeds approaching $\sim$450 km s^{-1}; (2) an inner disk spanning

$0.5 \lesssim r \lesssim 1.2$ pc; and (3) an outer disk extending to $r \sim 7$ pc. The two disks counter-rotate, and the kinematics of the inner disk agree with the H$_2$O megamaser disk mapped by the VLBA (Greenhill & Gwinn 1997). The outer disk shows a Keplerian rotation curve consistent with an extrapolation of the rotation curve of the inner disk. We also find that the HCN radial velocity field is more complex along the molecular outflow axis, which suggests that we are also detecting but not fully resolving HCN emission associated with the outflow.

Conservation of angular momentum precludes the formation of counter-rotating disks out of a single epoch of accreting gas, and, to our knowledge, accretion disk warping mechanisms cannot induce counter-rotation (e.g., Tremaine & Davis 2014 and references therein). It seems likely that the counter-rotating outer disk formed from gas that has been more recently introduced to the >1 pc-scale environment, perhaps from an errant cloud falling out of the host galaxy or a captured satellite dwarf galaxy. Imanishi et al. (2018) demonstrated that the outer disk of the parsec-scale molecular torus also counter-rotates with respect to the molecular ring at 100 pc scales (see their Figure 1) and, we note, the sense of rotation of the galactic disk on kiloparsec scales (see, e.g., Helfer & Blitz 1995 and Brinks et al. 1997).

Because the central SMBH appears to dominate the gravitational potential in this region, the counter-rotating disks should be stable until, owing to dissipation, the outer disk starts

to collapse onto the inner disk. When that occurs, we would expect the outer disk to collapse on an orbital timescale, $t_{\rm orb} \sim 3 \times 10^4$ yr. The interaction between counter-rotating disks may enhance the accretion rate by one or two orders of magnitude (Kuznetsov et al. 1999; Nixon et al. 2012; Dyda et al. 2015). King & Pringle (2006, 2007) described a chaotic accretion scenario for the cosmological growth of black holes, namely, rapid accretion owing to randomly oriented and episodic accretion events. They cite the random orientation of Seyfert radio jets and ionization cones with respect to host galaxies as evidence for chaotic accretion (see Schmitt et al. 2003; Gallimore et al. 2006). In NGC 1068, we find direct evidence that the molecular obscuring medium consists of counter-rotating and misaligned disks on parsec scales.

ORCID iDs

C. M. Violette Impellizzeri https://orcid.org/0000-0003-4561-1713
Jack F. Gallimore https://orcid.org/0000-0002-6972-2760
Moshe Elitzur https://orcid.org/0000-0001-8143-3550
Dieter Lutz https://orcid.org/0000-0003-0291-9582
Alessandro Marconi https://orcid.org/0000-0002-9889-4238
Christopher P. O'Dea https://orcid.org/0000-0001-6421-054X

References

Antonucci, R. 1993, ARA&A, 31, 473
Antonucci, R. R. J., & Miller, J. S. 1985, ApJ, 297, 621
Astropy Collaboration, Robitaille, T. P., Tollerud, E. J., et al. 2013, A&A, 558, A33
Bland-Hawthorn, J., Gallimore, J. F., Tacconi, L. J., et al. 1997, Ap&SS, 248, 9
Briggs, D. 1995, PhD thesis, New Mexico Institute of Mining and Technology
Brinks, E., Skillman, E. D., Terlevich, R. J., et al. 1997, Ap&SS, 248, 23
Capetti, A., Macchetto, F., Axon, D. J., Sparks, W. B., & Boksenberg, A. 1995, ApJL, 452, L87
Cecil, G., Bland, J., & Tully, R. B. 1990, ApJ, 355, 70
Cornwell, T., & Fomalont, E. B. 1989, ASPC, 6, 185
Cotton, W. D., Jaffe, W., Perrin, G., et al. 2008, A&A, 477, 517
Das, V., Crenshaw, D. M., Kraemer, S. B., et al. 2006, AJ, 132, 620
Dyda, S., Lovelace, R. V. E., Ustyugova, G. V., Romanova, M. M., & Koldoba, A. V. 2015, MNRAS, 446, 613
Gallimore, J. F., Axon, D. J., O'Dea, C. P., Baum, S. A., & Pedlar, A. 2006, AJ, 132, 546
Gallimore, J. F., Baum, S. A., & O'Dea, C. P. 1997, Natur, 388, 852
Gallimore, J. F., Baum, S. A., & O'Dea, C. P. 2004, ApJ, 613, 794
Gallimore, J. F., Baum, S. A., O'Dea, C. P., & Pedlar, A. 1996, ApJ, 458, 136
Gallimore, J. F., Elitzur, M., Maiolino, R., et al. 2016, ApJL, 829, L7
Gallimore, J. F., Henkel, C., Baum, S. A., et al. 2001, ApJ, 556, 694
Gallimore, J. F., & Impellizzeri, C. M. V. 2019, AJ, submitted
García-Burillo, S., Combes, F., Ramos Almeida, C., et al. 2016, ApJL, 823, L12
Greenhill, L. J., & Gwinn, C. R. 1997, Ap&SS, 248, 261
Helfer, T. T., & Blitz, L. 1995, ApJ, 450, 90
Hickox, R. C., & Alexander, D. M. 2018, ARA&A, 56, 625
Imanishi, M., Nakanishi, K., Izumi, T., & Wada, K. 2018, ApJL, 853, L25
Inglis, M. D., Young, S., Hough, J. H., et al. 1995, MNRAS, 275, 398
Kerr, F. J., & Westerhout, G. 1965, in Galactic Structure, ed. A. Blaauw & M. Schmidt (Chicage, IL: Univ. Chicago Press), 167
King, A. R., & Pringle, J. E. 2006, MNRAS, 373, L90
King, A. R., & Pringle, J. E. 2007, MNRAS, 377, L25
Kuznetsov, O. A., Lovelace, R. V. E., Romanova, M. M., & Chechetkin, V. M. 1999, ApJ, 514, 691
Lawrence, A., & Elvis, M. 1982, ApJ, 256, 410
Mason, R. E., Geballe, T. R., Packham, C., et al. 2006, ApJ, 640, 612
McMullin, J. P., Waters, B., Schiebel, D., Young, W., & Golap, K. 2007, in ASP Conf. Ser. 376, Astronomical Data Analysis Software and Systems XVI, ed. R. A. Shaw, F. Hill, & D. J. Bell (San Francisco, CA: ASP), 127
Muxlow, T. W. B., Pedlar, A., Holloway, A. J., Gallimore, J. F., & Antonucci, R. R. J. 1996, MNRAS, 278, 854
Nixon, C. J., King, A. R., & Price, D. J. 2012, MNRAS, 422, 2547
Osterbrock, D. E., & Shaw, R. A. 1988, ApJ, 327, 89
Ramos Almeida, C., & Ricci, C. 2017, NatAs, 1, 679
Sault, R. J., & Conway, J. E. 1999, ASPC, 180, 419
Schmitt, H. R., Donley, J. L., Antonucci, R. R. J., et al. 2003, ApJ, 597, 768
Tovmassian, H. M. 2001, AN, 322, 87
Tremaine, S., & Davis, S. W. 2014, MNRAS, 441, 140
van der Marel, R. P., & Franx, M. 1993, ApJ, 407, 525